Geophysical Research Letters®

Key Points:

- H_2O ice layers in Mars' Massive CO_2 Ice Deposit record obliquity-mediated rates of midlatitude-to-pole H_2O transport over the past 510 kyr
- The record's unique CO_2 cold-trapping environment isolates the orbit-forcing signal from other processes, simplifying its interpretation
- Orbit-resolved H_2O transport rates place an important new quantitative bound on processes driving Mars' recent (~3.5 Myr) global water cycle

A 510,000-Year Record of Mars' Climate

P. B. Buhler[1] 📍

[1]Planetary Science Institute, Tucson, AZ, USA

Abstract Mars' polar layered deposits record its climate history. However, no deposit yet analyzed provides a global water cycle record that can be tied to a specific orbital history. Here, I fill this gap by analyzing H_2O ice layer formation in Mars' south polar Massive CO_2 Ice Deposit (MCID), a 510,000-year climate record. Statistical analyses of ~10^9 formation model runs compared to observed stratigraphy indicate a variable H_2O deposition rate of ~1, 0.1, and 0.01 mm yr^{-1} at 20, 24, and 28° obliquity, respectively—likely recording the obliquity-dependent midlatitude-to-pole H_2O transport rate. The MCID record allows unprecedented obliquity-driven H_2O ice deposition rate derivation because of its well-defined age relative to other deposits and its CO_2 cold-trapping effect, which simplifies local seasonal and long-term H_2O flux. The recovery of an orbit-resolved H_2O transport rate is an essential step in elucidating Mars' global, orbit-driven water cycle.

Plain Language Summary Mars' south pole hosts a deposit of alternating CO_2 and H_2O ice layers, which contain a record of global H_2O and CO_2 transport as Mars' orbit evolved during the past 510 thousand years. I created a numerical model to simulate the build-up of the layers over time and ran the model approximately one billion times, each time using a different governing function of H_2O ice deposition as a function of Mars' orbital configuration. Using statistical analysis, I found that an H_2O ice deposition function that exponentially decreases as a function of obliquity (spin-axis tilt) best recreates the observed layer sequence. Recovery of a south polar H_2O-ice-deposition-versus-obliquity function is novel and important for elucidating how Mars' global water cycle is driven by its orbital variations.

1. Introduction

Characterizing the history of processes controlling Mars' recent climate under different orbital configurations is a major Mars science goal (Banfield et al., 2020). Mars' polar deposits contain a record of H_2O transport between north and south polar, mid-latitude, and equatorial reservoirs in response to Mars' orbital element oscillations (Becerra et al., 2021; Smith et al., 2020).

4–5 Myr ago, a 10(+)-Myr duration high obliquity state favoring tropical H_2O glaciation (Head et al., 2003) transitioned to a low obliquity state (Laskar et al., 2004). Within <~1 Myr, tropical H_2O ice migrated to the midlatitudes and poles (Montmessin et al., 2004), followed by gradual transport of midlatitude H_2O ice to the poles (Levrard et al., 2007; Mellon & Jakosky, 1995).

Mars' recent (<~3.5 Myr) H_2O cycle is probably driven by 10^5-yr obliquity and 10^4-yr longitude of perihelion cycles. Midlatitude-to-pole H_2O transport is likely obliquity mediated, but quantitative present-day and historical transport rates are highly uncertain (Montmessin et al., 2017). Interhemispheric polar H_2O ice transport is likely mediated by longitude of perihelion precession; Mars' present configuration favors north-to-south polar H_2O ice transport, reversing at opposite perihelion configuration (Montmessin et al., 2007). However, the CO_2 south polar residual cap (SPRC) is a perennial cold-trap sink of H_2O (Richardson & Wilson, 2002). Presently, ~3×10^{12} kg of H_2O ice participates in an equilibrated seasonal sublimation-deposition cycle. Approximately one-third exchanges between hemispheres and ~two-thirds recycles within the northern hemisphere (Montmessin et al., 2017).

Previous studies of H_2O ice and dust layers in the North and South Polar Layered Deposits (NPLD, SPLD) and near-polar ice deposits extracted ~0.1–0.5 mm yr^{-1} deposition rates averaged over a few Myr using wavelet analysis (Becerra et al., 2017, 2019; Sori et al., 2022) and simplified stratigraphic development modeling (Hvidberg et al., 2012). However, these averaging timescales are much longer than orbital element periodicities, the deposits have loose temporal constraints (Tanaka et al., 2008), and no model has yet produced a one-to-one correlation between modeled and observed layers in these deposits (Hvidberg et al., 2012; Levrard et al., 2007). Thus, quantitative transport rates as a function of Mars' orbital configuration along any leg of Mars' global H_2O cycle have remained elusive.
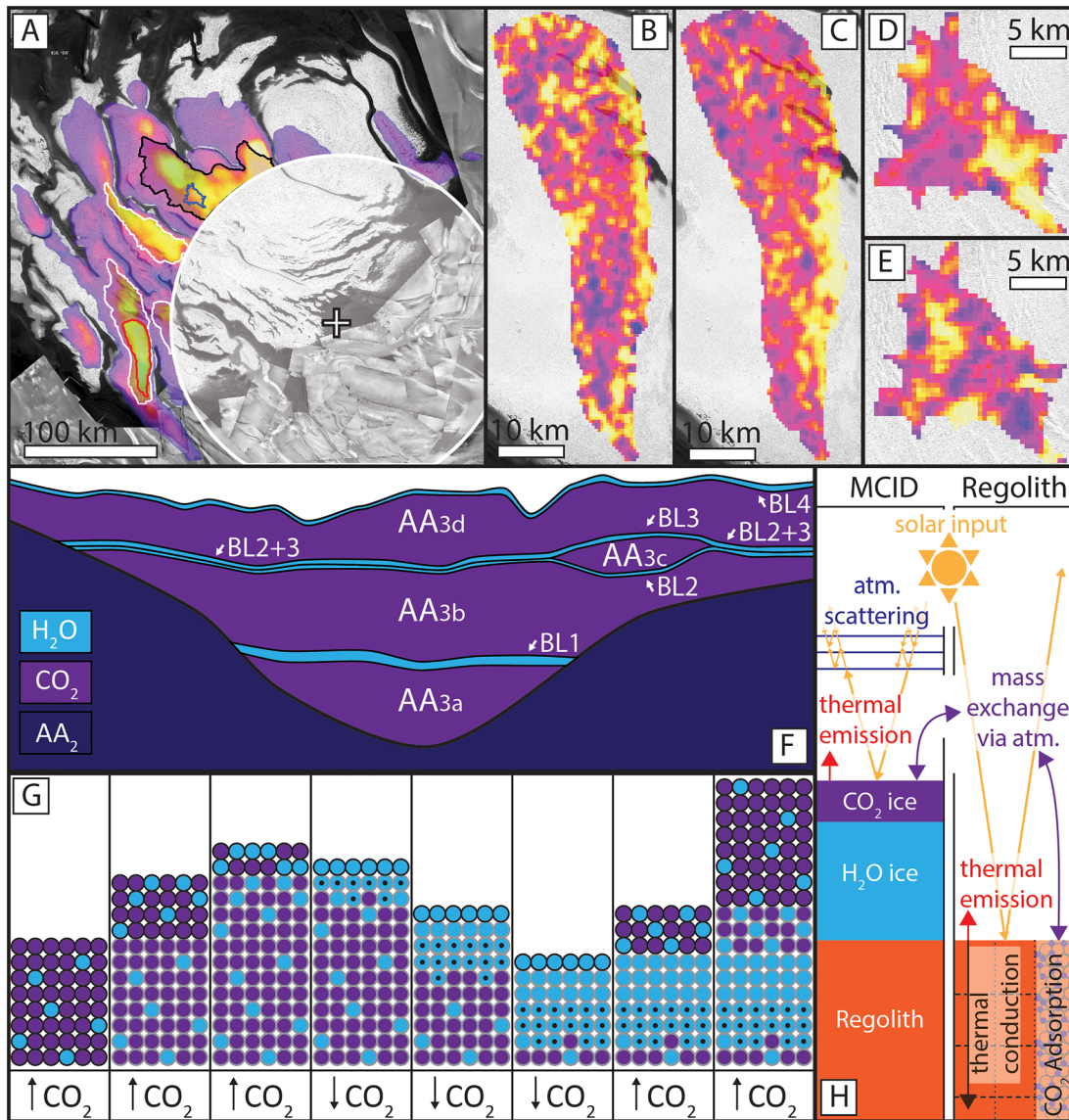
Figure 1. (a) Massive CO_2 Ice Deposit overview: pole (cross); no RADAR observations poleward of 87°S (white circle); 0°E (up), 90°E (right); colourized MCID thickness (Alwarda & Smith, 2021); Bounding Layer unit outlines: blue (Region 2 "lens") = "BL3" overlying "BL2," black = "BL2+3," white = "BL2+3" (see Text S1 in Supporting Information S1 nomenclature), red (Region 1) = "BL1." On THEMIS mosaic (Edwards et al., 2011) and CTX mosaic (Thomas et al., 2016). (b) Thickness of BL1 and (c) BL2+3 in Region 1, (d) BL2 and (e) BL3 in Region 2 (Alwarda & Smith, 2021). Histogram equalized color ranges, cool colors = low, warm = high: (a) 0–946 m, (b) 6–50 m, (c) 16–55 m, (d) 14–71 m, (e) 23–69 m. (f) Schematic MCID cross section. AA_2 is dusty H_2O ice basement. (g) Schematic stratigraphic model; time marches left to right. Blue = H_2O unit volume, purple = CO_2 unit. Black outline = new deposition, black dot = consolidated from prior deposition higher in column. MCID CO_2 flux (increasing/decreasing) is noted. (h) Schematic global CO_2 model (left = polar ice, right = nonpolar regolith).

To address this knowledge gap, this study aims to determine south polar H_2O deposition rates as a function of Mars' orbital configuration in a previously unexplored record: H_2O ice layers embedded in Mars' south polar Massive CO_2 Ice Deposit (MCID; Bierson et al., 2016; Phillips et al., 2011; Figure 1). The MCID's mass approximately equals Mars' current, principally CO_2 atmosphere (Putzig et al., 2018) and contains spatially variable ~10s-meter-thick H_2O ice Bounding Layers (BLs), dividing the CO_2 ice into ~100s-meter-thick layers (Figure 1; Alwarda & Smith, 2021). The MCID formed through exchange between polar CO_2 ice, atmospheric CO_2, and CO_2 adsorbed in regolith ("soil"), driven by Mars' cyclic orbital evolution over the past 510 kyr (Figures 1h and 2; Buhler & Piqueux, 2021; Buhler et al., 2020). When obliquity decreases, polar sunlight decreases, and the MCID accumulates CO_2 ice (with H_2O ice and dust impurities). When obliquity increases, CO_2 ablates, leaving behind lag layers (i.e., BLs) of residual refractory material (H_2O ice, dust; Figure 1g).
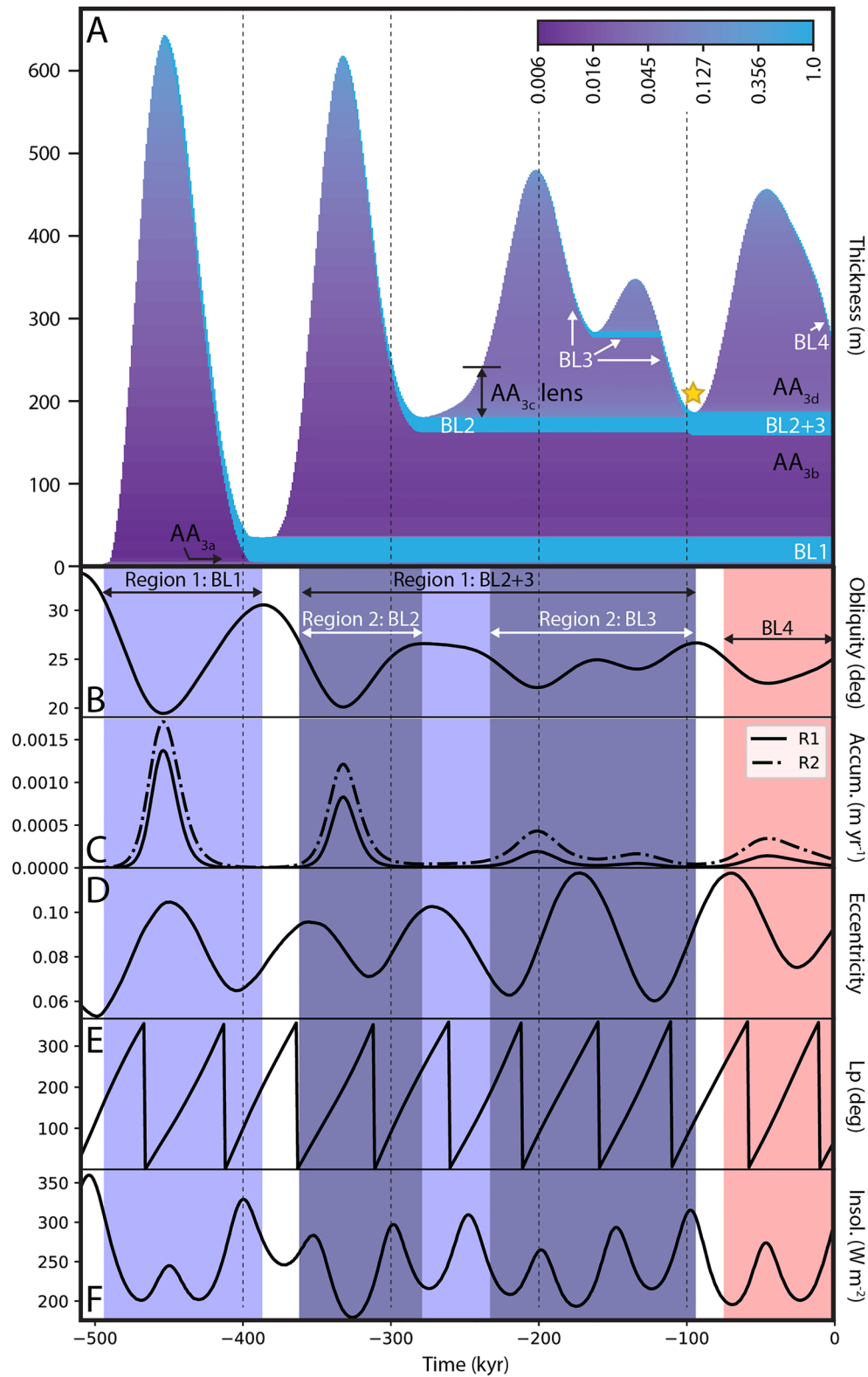
Figure 2.

The MCID record provides two main benefits over previously analyzed dusty H_2O ice stratigraphy. First, physics-based modeling (Buhler & Piqueux, 2021; Buhler et al., 2020) has reproduced observed CO_2 layers, so MCID layer ages are better known than other polar layers. Second, the MCID cold traps H_2O ice, meaning (a) H_2O ice depositional physics are simpler (e.g., Mischna et al., 2003) and (b) BLs likely experience negligible ablation (Buhler et al., 2020; Innannen et al., 2022), allowing deposition rate retrieval (rather than net accumulation plus ablation rates).

Previous MCID formation modeling simplistically assumed constant H_2O ice deposition (Buhler et al., 2020), predicting BL thicknesses inconsistent with later observation (Alwarda & Smith, 2021). Here, I introduce a new model of variable H_2O ice deposition onto the MCID, building on a model of CO_2 exchange between the MCID, atmosphere (Buhler et al., 2020), and regolith (Buhler & Piqueux, 2021).

I use Markov Chain Monte Carlo (MCMC) modeling to evaluate heuristic H_2O deposition rate (r_{H_2O}) functions of various orbital parameters. This approach permits high-flexibility, broad exploration of r_{H_2O} parameter space, such that models can fit observations unconstrained by prior, process-based expectations. This flexibility is important because of the vast number of unconstrained processes governing r_{H_2O} (e.g., Smith et al., 2020). Nevertheless, model reasonableness is assessed from a physical process standpoint. Crucially, however, process-based analysis is performed *a posteriori*, unlike previous approaches constraining r_{H_2O} *a priori* to physical processes, essentially yielding parameter optimization for r_{H_2O} (onto the NPLD) within single-function heuristics: an (approximate) polar insolation step function (Hvidberg et al., 2012; their Section 5.1) or quadratic accumulation and exponential ablation functions of obliquity (Levrard et al., 2007).

2. Methods

2.1. Global CO_2 Exchange and Stratigraphic Model

Model CO_2 ice flux and r_{H_2O} are calculated in 1-kyr timesteps, yielding an output 1-kyr-resolution time-marching MCID stratigraphic column (Figure 2a). CO_2 ice flux follows equilibrated, mass-conserved exchange between the MCID, atmosphere, and regolith, driven by obliquity-dependent latitudinal insolation (Figure 1h; Buhler and Piqueux (2021); Text S2 in Supporting Information S1). Briefly, MCID-atmosphere vapor pressure equilibrium is determined by MCID surface elevation and CO_2 ice temperature set by insolation (including surface reflection, emission, and atmospheric scattering). Regolith-atmosphere adsorption equilibrium is determined by calculating regolith temperature set by insolation (including surface reflection and emission and subsurface conduction) across a 2-dimensional (latitude-depth) grid and iteratively calculating atmospheric pressure and total regolith adsorption using an empirical pressure-temperature adsorption relation (Zent & Quinn, 1995) until convergence is reached. The MCID and regolith exchange indirectly via the atmosphere.

During CO_2 accumulation, H_2O ice deposits as an intimate mixture with thickness specified by an r_{H_2O} function (Section 2.2, Table 1). A new layer is added to the column top with appropriate fractional H_2O content and thickness equal to the sum of deposited CO_2 and H_2O ice layer thicknesses (Figure 1g). When CO_2 ablates, a pure H_2O ice layer grows at the column top from both (a) newly deposited H_2O ice and (b) previously deposited H_2O liberated from subliming CO_2 (Figure 1g). If CO_2 ice between two BLs completely ablates, they merge (Figure 2a).

Conceptually, new H_2O sources from the atmosphere, cold-trapped onto the main MCID body (during accumulation epochs) or onto a thin perennial CO_2 deposit overlying the topmost BL, that is, a "paleo-SPRC" (during ablation epochs; Buhler et al., 2020). H_2O ice depositing onto a paleo-SPRC settles to the topmost BL during regional paleo-SPRC accumulation-ablation cycles (Buhler et al., 2017; Thomas et al., 2016) over ∼100 years (Byrne & Ingersoll, 2003)—shorter than the model timestep—so r_{H_2O} is treated as direct deposition onto the model column.

Figure 2. (a) Favored model Region 1 stratigraphy. Log-normalized color bar shows fractional H_2O component. Star = BL2-BL3 merger. Nb. BL2 and BL3 are constrained not to merge in the Region 2 model (not shown except for AA$_{3c}$ label, see Section 2.3). (b) Obliquity, (c) favored model r_{H_2O}, (d) eccentricity, (e) longitude of perihelion, (f) peak annual 90°S insolation (B and D-F from Laskar et al., 2004). Lavender regions indicate deposition duration of material ultimately agglomerated into BL1 and BL2+3 in Region 1. Dark lavender regions indicate deposition duration of material ultimately agglomerated into BL2 and BL3 in Region 2. Red region indicates deposition duration of material ultimately agglomerated into BL4.

Table 1

Bayes Factor for All Models, as a Function of Obliquity ε, Eccentricity e, Longitude of Perihelion L_P, and Peak Annual South Polar Insolation I

Functional form (x indicates $\varepsilon, e, L_P,$ or I, respectively)	ε	e	L_P	I
Region 1 Constant: $r_{H_2O} = A_0$	1	1	1	1
Region 1 Linear: $r_{H_2O} = A_1 + B_1 x$	6	0.9	0.6	4
Region 1 Quadratic: $r_{H_2O} = A_2 + B_2 x + C_2 x^2$	65	29	0.9	64
Region 1 Cubic: $r_{H_2O} = A_3 + B_3 x + C_3 x^2 + D_3 x^3$	78	57	0.9	59
Region 1 Quartic: $r_{H_2O} = A_4 + B_4 x + C_4 x^2 + D_4 x^3 + E_4 x^4$	71	72	0.9	55
Region 1 Exponential (dec.): $r_{H_2O} = A_5 \times \exp(B_5 x)$	64	66	6	0.3
Region 1 Exponential (inc.): $r_{H_2O} = A_6 \times \exp(B_6 x)$	63	0.5	6	4
*Region 1 Step Function (dec.): $r_{H_2O} = \begin{cases} A_7, x \le B_7 \\ C_7, x > B_7 \end{cases}; A_7 > C_7$	0.5	40	0.7	1.1
*Region 1 Step Function (inc.): $r_{H_2O} = \begin{cases} A_8, x \ge B_8 \\ C_8, x < B_8 \end{cases}; A_8 < C_8$	17	0.9	0.7	52
Region 1 Cosine: $r_{H_2O} = A_9 \times \cos(B_9 + C_9 \times x) + D_9$	52	8	1.0	16
Region 1 Gaussian: $r_{H_2O} = A_{10} \times \exp\left(-(x - B_{10})^2/(2 \times C_{10}^2)\right)$	1.1	1.0	1.4	15
Region 2 Constant: $r_{H_2O} = A_0$	1	1	1	1
Region 2 Linear: $r_{H_2O} = A_1 + B_1 x$	1.2	1.0	1.1	1.0
Region 2 Quadratic: $r_{H_2O} = A_2 + B_2 x + C_2 x^2$	2.6	1.5	1.0	1.5
Region 2 Cubic: $r_{H_2O} = A_3 + B_3 x + C_3 x^2 + D_3 x^3$	1.5	1.6	1.0	2.2
Region 2 Quartic: $r_{H_2O} = A_4 + B_4 x + C_4 x^2 + D_4 x^3 + E_4 x^4$	2.7	1.2	0.9	2.3
Region 2 Exponential (dec.): $r_{H_2O} = A_5 \times \exp(B_5 x)$	21	0.5	1.9	1.7
Region 2 Exponential (inc.): $r_{H_2O} = A_6 \times \exp(B_6 x)$	<0.1	0.7	<0.1	0.9
*Region 2 Step Function (dec.): $r_{H_2O} = \begin{cases} A_7, x \le B_7 \\ 0, x > B_7 \end{cases}; A_7 > C_7$	1.7	1.1	1.2	1.2
*Region 2 Step Function (inc.): $r_{H_2O} = \begin{cases} A_8, x \ge B_8 \\ 0, x < B_8 \end{cases}; A_8 < C_8$	1.5	0.9	1.4	1.1
Region 2 Cosine: $r_{H_2O} = A_9 \times \cos(B_9 + C_9 \times x) + D_9$	1.3	1.4	1.0	1.1
Region 2 Gaussian: $r_{H_2O} = A_{10} \times \exp\left(-(x - B_{10})^2/(2 \times C_{10}^2)\right)$	1.0	1.0	1.1	1.0

Note. *For L_P the step function was cyclic modulo $360°$, that is, $r_{H_2O} = \begin{cases} A_N, x : [B_N, D_N] \\ C_N, x : (D_N, B_N) \end{cases}$.

2.2. Formal Best-Fit r_{H_2O} Determination

Various r_{H_2O} formulations dependent on obliquity, eccentricity, longitude of perihelion, or south polar insolation were considered (Table 1), chosen because they cover the range of previously proposed orbitally driven polar r_{H_2O}: polynomial and exponential (e.g., Levrard et al., 2007); step function (e.g., Hvidberg et al., 2012); cosine or Gaussian (i.e., periodic or peaked; Montmessin et al., 2007; Vos et al., 2022). All models have equal prior probability and all parameters have uniform prior probability. Each r_{H_2O} formulation model was run through a 10^8-iteration MCMC simulation (Buhler & Piqueux, 2021). Model likelihoods were compared using Bayes factors B, which reward better fits but penalize higher complexity (e.g., Kass & Raftery, 1995):

$$B_{i,j} = \frac{pr(\boldsymbol{D}|H_i)}{pr(\boldsymbol{D}|H_j)} \tag{1}$$

Model likelihood $pr(\boldsymbol{D}|H)$ is the average of likelihoods sampled at each MCMC m-indexed step (Kass & Raftery, 1995):

$$pr(\boldsymbol{D}|H_i) = \frac{1}{M}\sum_{m=1}^{M}\prod_{d=1}^{D}\frac{1}{\sqrt{2\pi\sigma_d^2}}\exp\left(-\frac{1}{2}\left(\frac{(z(\theta_m)-\mu_d)^2}{\sigma_d^2}\right)\right) \tag{2}$$

The righthand side is the likelihood product for mean μ and standard deviation σ of each d-indexed BL thickness datapoint and model-predicted thickness z from model parameters θ, assuming Gaussian variance.

2.3. Observed Stratigraphy

Models were fit to two regional observations (Figure 1a; Alwarda & Smith, 2021). Region 1 is near [86°S, 270°E], clipped to where BL2+3 overlies BL1 (Figures 1b and 1c); here, observed BL1 thickness is 31 ± 5 m and BL2+3 thickness is 30 ± 5 m. Region 2 is near [86°S, 315°E], clipped to where BL3 separably overlies BL2 (Figures 1d and 1e); here, observed BL2 thickness is 34 ± 8 m and BL3 thickness is 37 ± 7 m. Quoted uncertainty is the quadratic addition of 10-m vertical Shallow Radar (SHARAD) instrument resolution (Foss et al., 2017; Seu et al., 2007; divided by $\sqrt{N}$, for $N = 4{,}436$ and 909 observations in Region 1 and 2, respectively) and BL lateral thickness variation. These regions are the only regions with multiple overlying BLs, and therefore the only regions permitting meaningful assessment of non-constant deposition models.

SHARAD non-observation of BL4 was accounted for via an equal probability prior of BL4 ≤ 10 m (SHARAD's resolving power) and Gaussian prior probability decrease with 1-σ scale of 5 m for BL4 > 10 m; equivalently, the prior assumes BL4 has a 50%, 68%, 95%, or 99% likelihood of being resolved if it were 10, 15, 20, or 25 m thick, respectively. Region 2 modeling assumes H_2O ice within the 60 m of CO_2 directly above BL2 remains trapped within the CO_2 ice (i.e., average AA_{3c} lens thickness (Alwarda & Smith, 2021)).

3. Results

Table 1 shows model Bayes factors B, relative to a constant deposition model. B standard interpretation is 1-to-3: "marginal," 3-to-20: "positive," 20-to-150: "strong," and >150: "very strong" (Kass & Raftery, 1995). In Region 2, exponentially decreasing r_{H_2O}-versus-obliquity ε is "strongly" (B = 21) favored over a constant r_{H_2O} model; all other models yield only marginal improvement ($B < 3$). In Region 1, exponentially decreasing r_{H_2O}-versus-ε (B = 64) is also "strongly" favored. However, quadratic r_{H_2O}-versus-ε, eccentricity e, and peak annual south polar insolation I; exponential r_{H_2O}-versus-e; cosine r_{H_2O}-versus-ε; step-function r_{H_2O}-versus-e; and Gaussian r_{H_2O}-versus-I, are also "strongly" favored. Evidence for higher order polynomial models is statistically non-significant ($B << 3\times$) compared to the lower polynomial forms nested within them; they are therefore formally disfavored (e.g., Raftery, 1993). All model solutions are presented in Figures S1–S8 in Supporting Information S1.

B alone does not distinguish between Region 1 "strongly" favored models. However, the similarity of the model solutions with exponentially decreasing r_{H_2O}-versus-ε in Region 1 and Region 2 (Figure 3a) indicate preferring this solution, discussed further in Sections 4.1 and 4.2. Favored Region 1 $r_{H_2O} = \exp(-0.7450 \times \varepsilon + 14.80)$ and Region 2 $r_{H_2O} = \exp(-0.5171 \times \varepsilon + 10.59)$ (Figure 3a).

Favored Region 1 r_{H_2O} history (Figure 2c) and resultant model stratigraphy (Figure 2a) predict BL1 thickness = $30.4^{+7.3}_{-6.6}$, BL2+3 thickness = $28.3^{+7.3}_{-7.8}$, BL4 thickness = $6.3^{+2.4}_{-2.3}$ m and modern day ($\varepsilon = 25.2°$) r_{H_2O} = $0.03^{+0.03}_{-0.02}$ mm yr^{-1} (68% confidence intervals). The favored Region 2 model predicts a generally similar (but higher) r_{H_2O}-versus-ε relation (Figures 2c and 3a), BL2 thickness = $33.8^{+7.0}_{-7.8}$, BL3 thickness = $25.6^{+5.0}_{-5.1}$, BL4 thickness = $17.2^{+3.1}_{-3.0}$ m and modern day r_{H_2O} = $0.09^{+0.02}_{-0.03}$ mm yr^{-1}.

4. Discussion

4.1. Model Performance Interpretation

Model selection behavior can be understood within the following framework. In Region 1, BL1 and BL2+3 thicknesses are similar, but BL2+3 formed over 2.4× as much time (387-to-94 kyr) as BL1 (510-to-387 kyr;
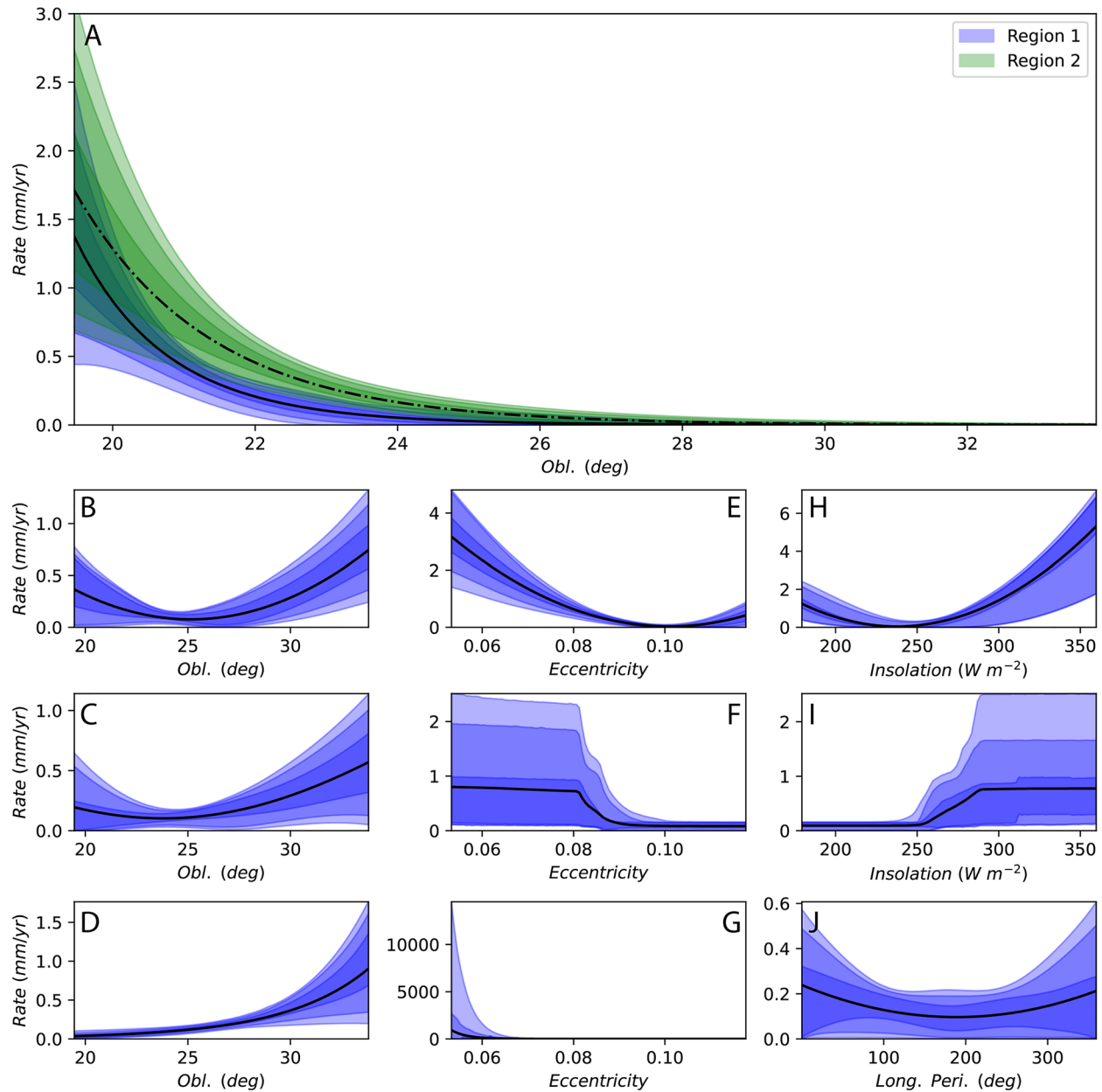
Figure 3. Model Massive CO_2 Ice Deposit water ice deposition r_{H_2O} with best fit (line), 68% (dark), 95% (intermediate), and 99% (light) confidence intervals. (a) Favored Region 1 (blue/solid) and 2 (green/dash-dot) models: exponential decrease with ε. Other Region 1 models: (b) quadratic, (c) cosine, (d) exponential increase with ε; (e) quadratic, (f) decreasing step function, (g) exponential decrease with e; (h) quadratic, (i) increasing step function with I; (j) quadratic with L_P.

Figure 2). Likewise, in Region 2, BL2 and BL3 thicknesses are similar, but BL3 formed over 1.7× as much time (238-to-94 kyr) as BL2 (362-to-278 kyr). Thus, selection favors models with ∼2.4× higher aggregate r_{H_2O} during BL1 formation than during BL2+3 formation in Region 1 and ∼1.7× higher r_{H_2O} during BL2 formation than during BL3 formation in Region 2.

For example, ε variation amplitudes during BL1 formation were higher than during BL2+3 formation yet oscillated around a ∼24° center during both periods (Figure 2b). Thus, Region 1 r_{H_2O}-versus-ε models degenerately prefer high r_{H_2O} at low ε (Figure 3a), high ε (Figure 3d) or both (with minimum r_{H_2O} centered at $\varepsilon \sim 24°$; Figures 3b and 3c) because these solutions yield higher r_{H_2O} during BL1 formation than during BL2+3 formation. Generally, solutions maximize r_{H_2O} for orbital parameter space more represented during BL1 formation versus BL2+3 formation, as evident by comparing Figure 3 solutions vis-à-vis Figure 2 orbital history.

Region 2 yields a single "strongly" favored exponential r_{H_2O}-versus-ε functional form. For Region 1, exponential r_{H_2O}-versus-ε is also "strongly" favored, but alongside other forms. Solutions for Region 1 are likely more degenerate because Region 1 samples longer deposition periods than Region 2, averaging out r_{H_2O} temporal variations sampled by the BLs, thereby decreasing signal uniqueness. Based on Region 2 fit *a posteriori* information, I favor exponentially increasing r_{H_2O}-versus-ε over other equally performing (based solely on *B*) functions for Region 1 because it is difficult to conceive of processes driving r_{H_2O} according to different orbital dependencies in two nearby, physically similar environments.

Additionally, other Region 1 solutions are inconsistent with physics-based H_2O cycle predictions. Quadratic, cosine, and exponentially increasing r_{H_2O}-versus-ε and step function r_{H_2O}-versus-I solutions (Figures 3b–3d, and 3i) have increasing r_{H_2O} for $\varepsilon > \sim 24°$, opposite to physics-based modeling (e.g., Toon et al., 1980). Potentially, increased dust deposition augmenting r_{H_2O} could thicken BLs at high ε or I, but Section 3 results would require significantly larger high-ε deposition rates than seen in dust cycle modeling (Emmett et al., 2020). The quadratic r_{H_2O}-versus-L_P solution (Figure 3j) is equally distributed around a constant value at the 1σ level, indicating weak L_P dependence. Furthermore, the mean solution indicates $\sim 180°$ minimum and $\sim 0°$ maximum r_{H_2O}, $90°$ out of phase with physics-based modeling (Montmessin et al., 2007). Other "strongly" favored solutions (Figures 3e–3h) have neither obvious physical meaning nor correlate with behavior found in prior studies.

4.2. Regional Differences

Unique to Region 1, BL1 overlies CO_2 ice Unit AA_{3a} (Figure 1f), elsewhere BL1 is not separately resolvable from Unit AA_2 basement (Figure 1a). Two mechanisms may be responsible for preserving Region 1 Unit AA_{3a}: (a) Region 1's lower elevation provides greater CO_2 stability given equivalent surface thermal and optical properties (Buhler et al., 2020) and (b) Region 1 overlies a subsurface basin, which potentially ponded a thick Unit AA_{3a} layer via glacial flow (Smith et al., 2022).

Unique to Region 2, BL2 and BL3 separate around CO_2 ice Unit AA_{3c} (Figure 1f), indicating incomplete Unit AA_{3c} ablation during the ε maximum at 94 kyr (Figure 2). Also, Region 2 BL2 + BL3 thickness is greater than merged BL2+3 thickness elsewhere (Alwarda & Smith, 2021). Notably, the 94-kyr ($26.67°$) and 278-kyr obliquity maxima ($26.60°$) were similar (Figure 2b), indicating local, second-order (compared to ε control) mechanical or thermal kinetic hindrance due to the unusually thick overlying BL3 layer may have protected Unit AA_{3c} CO_2 from complete ablation, even though BLs do not generally protect against subsurface CO_2 sublimation (Buhler et al., 2020).

Figure 3a shows that model-predicted regional rates of change in r_{H_2O} as a function of ε are remarkably similar, but that r_{H_2O} is consistently higher in Region 2 (with formal statistical significance; Text S3 in Supporting Information S1). Wind-mediated water transport variation may cause local r_{H_2O} differences, as seen for 1-to-100-km scales in the NPLD, SPLD, and Antarctic (Earth) records (e.g., Herny et al., 2014; Smith et al., 2013) and present-day south polar r_{H_2O} observation and modeling (Langevin et al., 2007; Montmessin et al., 2004, 2007; Pottier et al., 2017). Persistently different regional deposition rates may be related to local or global orographic effects, such as known asymmetrical CO_2 (Colaprete et al., 2005) and H_2O (Langevin et al., 2007) south polar deposition patterns driven by Hellas Basin.

4.3. Previous r_{H_2O} Calculations

Model-predicted present-day ($\varepsilon = 25.2°$) r_{H_2O} (Section 3) is consistent with observation and physics-based modeling. Brown et al. (2014) observed $r_{H_2O} = 6 \times 10^{12}$ to 1.2×10^{14} g yr^{-1} deposition onto the SPRC, commensurate, at the low end, with Region 1 and Region 2 present-day, model-predicted $r_{H_2O} = 4.5^{+6.0}_{-4.0} \times 10^{12}$ g yr^{-1} and $1.7^{+0.3}_{-0.6} \times 10^{13}$ g yr (calculated by extrapolation over a 2×10^{11} m^2 cap area, as in Brown et al. (2014)). Langevin et al. (2007) climate modeling predicts present-day r_{H_2O} between several $\times 0.1$—to—1 micron per sol between solar longitudes 189 and 270° (their Figure 28), equivalent to a few $\times 10^{12} - 2 \times 10^{13}$ g yr^{-1} (scaled to 2×10^{11} m^2, as above), consistent with Section 3 results. Earlier climate modeling by Richardson and Wilson (2002, their Figure 12c) and Mischna et al. (2003, their Figure 11a) both find slightly higher $r_{H_2O} \sim 6$–9×10^{13} g yr^{-1} and $\sim 7 \times 10^{13}$ g yr^{-1}, respectively (scaled to 2×10^{11} m^2, as above).

Myr-average H_2O-ice-plus-dust deposition rates calculated from the SPLD (from $>\sim 10$ Myr ago; Becerra et al., 2019), Burroughs crater (~ 0–4.5 Myr; $72.3°$S, $116.6°$E; Sori et al., 2022), and NPLD (~ 0–4.5 Myr; e.g.,

Hvidberg et al., 2012; Becerra et al., 2017) records are 0.13–0.39, 0.13, and 0.55 mm yr^{-1}, respectively. Section 3 best-fit equations yield a comparable average 510-kyr MCID r_{H_2O} = 12 mm yr^{-1} (Region 1) and 0.25 mm yr^{-1} (Region 2). Extrapolating to 1 or 4.5 Myr yields higher MCID r_{H_2O} ($\sim$1.0 mm yr^{-1}) due to substantial sampling of low-ε (15–19°) r_{H_2O}. However, exponential r_{H_2O} extrapolation beyond ε sampled by BLs ($\sim$19–34°) should be interpreted cautiously.

4.4. Physical Interpretation

Perennial (SPRC or MCID) CO_2 ice cold traps atmospheric water entering MCID airspace (e.g., Montmessin et al., 2007). Thus, MCID r_{H_2O} has a straightforward interpretation: the rate of atmospheric water entering MCID airspace, a much simpler interpretation than r_{H_2O} onto other (non-perennially-CO_2-covered) polar deposits, which is the net result of a complex, incompletely understood seasonal H_2O accumulation-ablation cycle (e.g., Hvidberg et al., 2012). Moreover, MCID H_2O ice remains cold-trapped until ε exceeds $\sim$34° (Buhler & Piqueux, 2021), the threshold at which the entire MCID ablates (and BLs merge onto underlying SPLD and ablate until a thick enough protective dust lag develops (e.g., Herkenhoff & Plaut, 2000)). Thus, MCID r_{H_2O} records a straightforward accumulation rate, as opposed to the complex seasonally and orbitally varying accumulation-ablation signal in other layered ice deposits (e.g., Becerra et al., 2017).

Water entering MCID airspace ultimately sources from north polar and/or midlatitude regolith reservoirs (e.g., Montmessin et al., 2017). Recent ($<\sim$3.5 Myr) global H_2O exchange is likely controlled by 10^5-yr (ε-dependent) midlatitude-to-pole H_2O ice exchange and 10^4-yr (L_P-dependent) interhemispheric polar H_2O ice exchange (Section 1). Interhemispheric exchange transfers H_2O away from the hemisphere with short, hot summers (presently south-to-north) (Montmessin et al., 2007). L_P circulates on shorter (51 kyr; Laskar et al., 2004) timescales than BL formation, averaging out L_P-dependent r_{H_2O} variation (Figure 2e). Consequently, this study neither finds nor rules out meaningful r_{H_2O}-versus-L_P or r_{H_2O}-versus-I dependency. However, r_{H_2O}-versus-ε signal recovery (Figure 3a) indicates that r_{H_2O}-versus-L_P variations do not obscure the r_{H_2O}-versus-ε relation.

Mars' polar and atmospheric reservoirs are mixed by seasonal and 51 kyr L_P cycles, which are shorter than ε cycles, so the ε-dependent r_{H_2O} result (Figure 3a) thus likely probes regolith processes governing midlatitude-to-pole H_2O transport (e.g., Mellon & Jakosky, 1995). Physics-based modeling also indicates increased midlatitude-to-pole transport with decreasing ε (Mischna et al., 2003; Schorghofer & Forget, 2012). However, midlatitude ice sublimation rates sensitively depend on unknown regolith properties (e.g., porosity, tortuosity) and are uncertain at order-of-magnitude levels, even for the present day (e.g., Montmessin et al., 2017), so the results presented here provide a major improvement in determining quantitative ε-mediated midlatitude-to-pole H_2O transport rates.

4.5. Future Work and Conclusion

Future BL4 thickness and BL ice-to-dust ratio observations will allow application of the techniques introduced here to more regions of the MCID and allow isolation of H_2O and dust deposition rates. In this work, I was chosen as a physically meaningful orbital element (ε, L_P, e) convolution that has been previously proposed to modulate r_{H_2O}; other convolutions could be considered in future work. Glacial flow in Region 2 is probably low, but is likely more significant in Region 1 (Smith et al., 2022) and future investigation of how flow affects r_{H_2O} interpretation will be useful.

The obliquity-dependent MCID H_2O deposition rates presented here provide new, quantitative insight into the recent, exogenous (orbital) driving of midlatitude-to-pole H_2O transport. Previous orbit-driven r_{H_2O} climate model investigations had either low parameter space resolution (e.g., Mischna et al., 2003) or studied conditions different from the past $\sim$3.5 Myr, for example, with large equatorial ice reservoirs (Levrard et al., 2004; Montmessin et al., 2004; Vos et al., 2022) or without a perennial CO_2 deposit (Emmett et al., 2020), while previous observational analysis derived only Myr-average polar deposition rates (Section 4.3). Thus, the results presented here provide a substantially improved framework for future quantitative investigations of endogenous processes driving Mars' recent ($\sim$3.5 Myr) global water cycle.

Data Availability Statement

Stratigraphic model code (version 1) and data plotted in Figures 2 and 3 are available in a figshare repository via https://doi.org/10.6084/m9.figshare.21201199.v1 under CC BY 4.0 license (Buhler, 2022); radar data (Figure 1) is available from Alwarda and Smith (2021).

References

Alwarda, R., & Smith, I. B. (2021). Stratigraphy and volumes of the units within the massive carbon dioxide ice deposits of Mars. *Journal of Geophysical Research: Planets*, *126*(5), e2020JE006767. https://doi.org/10.1029/2020je006767

Banfield, D., Stern, J., Davila, A., Johnson, S. S., Brain, D., Wordsworth, R., et al. (2020). *Mars science goals, objectives, investigations, and priorities: 2020 version*. Mars Exploration Program Analysis Group (MEPAG).

Becerra, P., Smith, I. B., Hibbard, S., Andres, C., Bapst, J., Bramson, A. M., et al. (2021). Past, present, and future of Mars polar science: Outcomes and outlook from the 7th international conference on Mars polar science and exploration. *The Planetary Science Journal*, *2*(5), 209. https://doi.org/10.3847/psj/ac19a5

Becerra, P., Sori, M. M., & Byrne, S. (2017). Signals of astronomical climate forcing in the exposure topography of the North Polar Layered Deposits of Mars. *Geophysical Research Letters*, *44*(1), 62–70. https://doi.org/10.1002/2016gl071197

Becerra, P., Sori, M. M., Thomas, N., Pommerol, A., Simioni, E., Sutton, S. S., et al. (2019). Timescales of the climate record in the south polar ice cap of Mars. *Geophysical Research Letters*, *46*(13), 7268–7277. https://doi.org/10.1029/2019gl083588

Bierson, C. J., Phillips, R. J., Smith, I. B., Wood, S. E., Putzig, N. E., Nunes, D., & Byrne, S. (2016). Stratigraphy and evolution of the buried CO_2 deposit in the Martian south polar cap. *Geophysical Research Letters*, *43*(9), 4172–4179. https://doi.org/10.1002/2016gl068457

Brown, A. J., Piqueux, S., & Titus, T. N. (2014). Interannual observations and quantification of summertime H_2O ice deposition on the Martian CO_2 ice south polar cap. *Earth and Planetary Science Letters*, *406*, 102–109. https://doi.org/10.1016/j.epsl.2014.08.039

Buhler, P. B. (2022). Data tables for water deposition rates onto Mars' South Polar massive CO_2 ice deposit (Buhler). Dataset. *Figshare*. https://doi.org/10.6084/m9.figshare.21201199.v1

Buhler, P. B., Ingersoll, A. P., Ehlmann, B. L., Fassett, C. I., & Head, J. W. (2017). How the Martian residual south polar cap develops quasi-circular and heart-shaped pits, troughs, and moats. *Icarus*, *286*, 69–93. https://doi.org/10.1016/j.icarus.2017.01.012

Buhler, P. B., Ingersoll, A. P., Piqueux, S., Ehlmann, B. L., & Hayne, P. O. (2020). Coevolution of Mars's atmosphere and massive south polar CO_2 ice deposit. *Nature Astronomy*, *4*(4), 364–371. https://doi.org/10.1038/s41550-019-0976-8

Buhler, P. B., & Piqueux, S. (2021). Obliquity-driven CO_2 exchange between Mars' atmosphere, regolith, and polar cap. *Journal of Geophysical Research: Planets*, *126*(5), e2020JE006759. https://doi.org/10.1029/2020je006759

Byrne, S., & Ingersoll, A. P. (2003). Martian climatic events on timescales of centuries: Evidence from feature morphology in the residual south polar ice cap. *Geophysical Research Letters*, *30*(13), 1696. https://doi.org/10.1029/2003gl017597

Colaprete, A., Barnes, J. R., Haberle, R. M., Hollingsworth, J. L., Kieffer, H. H., & Titus, T. N. (2005). Albedo of the South Pole on Mars determined by topographic forcing of atmosphere dynamics. *Nature*, *435*(7039), 184–188. https://doi.org/10.1038/nature03561

Edwards, C. S., Nowicki, K. J., Christensen, P. R., Hill, J., Gorelick, N., & Murray, K. (2011). Mosaicking of global planetary image datasets: 1. Techniques and data processing for thermal emission imaging system (THEMIS) multi-spectral data. *Journal of Geophysical Research*, *116*(E10), E10008. https://doi.org/10.1029/2010JE003755

Emmett, J. A., Murphy, J. R., & Kahre, M. A. (2020). Obliquity dependence of the formation of the Martian polar layered deposits. *Planetary and Space Science*, *193*, 105047. https://doi.org/10.1016/j.pss.2020.105047

Foss, F. J., Putzig, N. E., Campbell, B. A., & Phillips, R. J. (2017). 3D imaging of Mars' polar ice caps using orbital radar data. *The Leading Edge*, *36*(1), 43–57. https://doi.org/10.1190/tle36010043.1

Head, J. W., Mustard, J. F., Kreslavsky, M. A., Milliken, R. E., & Marchant, D. R. (2003). Recent ice ages on Mars. *Nature*, *426*(6968), 797–802. https://doi.org/10.1038/nature02114

Herkenhoff, K. E., & Plaut, J. J. (2000). Surface ages and resurfacing rates of the polar layered deposits on Mars. *Icarus*, *144*(2), 243–253. https://doi.org/10.1006/icar.1999.6287

Herny, C., Massé, M., Bourgeois, O., Carpy, S., Le Mouélic, S., Appéré, T., et al. (2014). Sedimentation waves on the Martian North Polar cap: Analogy with megadunes in Antarctica. *Earth and Planetary Science Letters*, *403*, 56–66. https://doi.org/10.1016/j.epsl.2014.06.033

Hvidberg, C. S., Fishbaugh, K. E., Winstrup, M., Svensson, A., Byrne, S., & Herkenhoff, K. E. (2012). Reading the climate record of the Martian polar layered deposits. *Icarus*, *221*(1), 405–419. https://doi.org/10.1016/j.icarus.2012.08.009

Innanen, A. C., Landis, M. E., Hayne, P. O., & Moores, J. E. (2022). Possible atmospheric water vapor contribution from Martian Swiss cheese terrain. *The Planetary Science Journal*, *3*(10), 242. https://doi.org/10.3847/psj/ac979e

Kass, R. E., & Raftery, A. E. (1995). Bayes factors. *Journal of the American Statistical Association*, *90*(430), 773–795. https://doi.org/10.1080/01621459.1995.10476572

Langevin, Y., Bibring, J. P., Montmessin, F., Forget, F., Vincendon, M., Douté, S., et al. (2007). Observations of the south seasonal cap of Mars during recession in 2004–2006 by the OMEGA visible/near-infrared imaging spectrometer on board Mars Express. *Journal of Geophysical Research*, *112*(E8), E08S12. https://doi.org/10.1029/2006je002841

Laskar, J., Correia, A. C. M., Gastineau, M., Joutel, F., Levrard, B., & Robutel, P. (2004). Long term evolution and chaotic diffusion of the insolation quantities of Mars. *Icarus*, *170*(2), 343–364. https://doi.org/10.1016/j.icarus.2004.04.005

Levrard, B., Forget, F., Montmessin, F., & Laskar, J. (2004). Recent ice-rich deposits formed at high latitudes on Mars by sublimation of unstable equatorial ice during low obliquity. *Nature*, *431*(7012), 1072–1075. https://doi.org/10.1038/nature03055

Levrard, B., Forget, F., Montmessin, F., & Laskar, J. (2007). Recent formation and evolution of northern Martian polar layered deposits as inferred from a Global Climate Model. *Journal of Geophysical Research*, *112*(E6), E06012. https://doi.org/10.1029/2006je002772

Mellon, M. T., & Jakosky, B. M. (1995). The distribution and behavior of Martian ground ice during past and present epochs. *Journal of Geophysical Research*, *100*(E6), 11781–11799. https://doi.org/10.1029/95je01027

Mischna, M. A., Richardson, M. I., Wilson, R. J., & McCleese, D. J. (2003). On the orbital forcing of Martian water and CO_2 cycles: A general circulation model study with simplified volatile schemes. *Journal of Geophysical Research*, *108*(E6), 5062. https://doi.org/10.1029/2003je002051

Montmessin, F., Forget, F., Rannou, P., Cabane, M., & Haberle, R. M. (2004). Origin and role of water ice clouds in the Martian water cycle as inferred from a general circulation model. *Journal of Geophysical Research*, *109*(E10), E10004. https://doi.org/10.1029/2004je002284

Montmessin, F., Haberle, R. M., Forget, F., Langevin, Y., Clancy, R. T., & Bibring, J. P. (2007). On the origin of perennial water ice at the South Pole of Mars: A precession-controlled mechanism? *Journal of Geophysical Research*, *112*(E8), E08S17. https://doi.org/10.1029/2007je002902

Montmessin, F., Smith, M. D., Langevin, Y., Mellon, M. T., & Fedorova, A. (2017). The water cycle. *The atmosphere and climate of Mars*, *18*, 338.

Phillips, R. J., Davis, B. J., Tanaka, K. L., Byrne, S., Mellon, M. T., Putzig, N. E., et al. (2011). Massive CO_2 ice deposits sequestered in the south polar layered deposits of Mars. *Science*, *332*(6031), 838–841. https://doi.org/10.1126/science.1203091

Pottier, A., Forget, F., Montmessin, F., Navarro, T., Spiga, A., Millour, E., et al. (2017). Unraveling the Martian water cycle with high-resolution global climate simulations. *Icarus*, *291*, 82–106. https://doi.org/10.1016/j.icarus.2017.02.016

Putzig, N. E., Smith, I. B., Perry, M. R., Foss, F. J., II., Campbell, B. A., Phillips, R. J., & Seu, R. (2018). Three-dimensional radar imaging of structures and craters in the Martian polar caps. *Icarus*, *308*, 138–147. https://doi.org/10.1016/j.icarus.2017.09.023

Raftery, A. E. (1993). *Bayesian model selection in structural equation models* (Vol. 154). Sage Focus Editions.

Richardson, M. I., & Wilson, R. J. (2002). Investigation of the nature and stability of the Martian seasonal water cycle with a general circulation model. *Journal of Geophysical Research*, *107*(E5), 5031. https://doi.org/10.1029/2001JE001536

Schorghofer, N., & Forget, F. (2012). History and anatomy of subsurface ice on Mars. *Icarus*, *220*(2), 1112–1120. https://doi.org/10.1016/j.icarus.2012.07.003

Seu, R., Phillips, R. J., Biccari, D., Orosei, R., Masdea, A., Picardi, G., et al. (2007). SHARAD sounding radar on the Mars Reconnaissance Orbiter. *Journal of Geophysical Research*, *112*(E5), E05S05. https://doi.org/10.1029/2006JE002745

Smith, I. B., Hayne, P. O., Byrne, S., Becerra, P., Kahre, M., Calvin, W., et al. (2020). The holy grail: A road map for unlocking the climate record stored within Mars' polar layered deposits. *Planetary and Space Science*, *184*, 104841. https://doi.org/10.1016/j.pss.2020.104841

Smith, I. B., Holt, J. W., Spiga, A., Howard, A. D., & Parker, G. (2013). The spiral troughs of Mars as 2376 cyclic steps. *Journal of Geophysical Research: Planets*, *2377*(9), 1835–1857. https://doi.org/10.1002/jgre.20142

Smith, I. B., Schlegel, N. J., Larour, E., Isola, I., Buhler, P. B., Putzig, N. E., & Greve, R. (2022). Carbon dioxide ice glaciers at the South Pole of Mars. *Journal of Geophysical Research: Planets*, *127*(4), e2022JE007193. https://doi.org/10.1029/2022je007193

Sori, M. M., Becerra, P., Bapst, J., Byrne, S., & McGlasson, R. A. (2022). Orbital forcing of Martian climate revealed in a south polar outlier ice deposit. *Geophysical Research Letters*, *49*(6), e2021GL097450. https://doi.org/10.1029/2021gl097450

Tanaka, K. L., Rodriguez, J. A. P., Skinner, J. A., Jr., Bourke, M. C., Fortezzo, C. M., Herkenhoff, K. E., et al. (2008). North Polar Region of Mars: Advances in stratigraphy, structure, and erosional modification. *Icarus*, *196*(2), 318–358. https://doi.org/10.1016/j.icarus.2008.01.021

Thomas, P. C., Calvin, W., Cantor, B., Haberle, R., James, P. B., & Lee, S. W. (2016). Mass balance of Mars' residual south polar cap from CTX images and other data. *Icarus*, *268*, 118–130. https://doi.org/10.1016/j.icarus.2015.12.038

Toon, O. B., Pollack, J. B., Ward, W., Burns, J. A., & Bilski, K. (1980). The astronomical theory of climatic change on Mars. *Icarus*, *44*(3), 552–607. https://doi.org/10.1016/0019-1035(80)90130-x

Vos, E., Aharonson, O., Schörghofer, N., Forget, F., Millour, E., Rossi, L., et al. (2022). Stratigraphic and isotopic evolution of the Martian polar caps from paleo-climate models. *Journal of Geophysical Research: Planets*, *127*(3), e2021JE007115. https://doi.org/10.1029/2021je007115

Zent, A. P., & Quinn, R. C. (1995). Simultaneous adsorption of CO_2 and H_2O under Mars-like conditions and application to the evolution of the Martian climate. *Journal of Geophysical Research*, *100*(E3), 5341–5349. https://doi.org/10.1029/94je01899

References From the Supporting Information

Gary-Bicas, C. E., Hayne, P. O., Horvath, T., Heavens, N. G., Kass, D. M., Kleinböhl, A., et al. (2020). Asymmetries in snowfall, emissivity, and albedo of Mars' seasonal polar caps: Mars climate sounder observations. *Journal of Geophysical Research: Planets*, *125*(5), e2019JE006150. https://doi.org/10.1029/2019JE006150